The Xe-SiO2 system at moderate pressure and high temperature

C. Crépisson, Chrystèle Sanloup, M Blanchard, J Hudspeth, K. Glazyrin, F. Capitani

HAL Id: hal-02107610
https://hal.sorbonne-universite.fr/hal-02107610v1

Submitted on 7 Feb 2019 (v1), last revised 23 Apr 2019 (v2)

The Xe-SiO$_2$ system at moderate pressure and high temperature

C. Crépisson[1], C. Sanloup[1], M. Blanchard[2], J. Hudspeth[1], K. Glazyrin[3], F. Capitani[4]

[1] Sorbonne Université, CNRS, UMR 7193 - Institut des Sciences de la Terre de Paris (ISTeP), 4 place Jussieu, 75005, Paris, France

[2] Géosciences Environnement Toulouse (GET), Université de Toulouse, CNRS, IRD, UPS, 14 avenue Edouard Belin, 31400 Toulouse, France

[3] Deutsches Electronen-Synchrotron (DESY), Hamburg, Germany

[4] Synchrotron SOLEIL, L'Orme des Merisiers, Saint-Aubin, 91192 Gif-sur-Yvette, France

Corresponding author: Céline Crépisson (celinecrepisson@hotmail.fr)

Key points

- The Xe-SiO$_2$ system is studied by *in situ* high pressure and temperature experiments and *ab initio* calculations.

- Xe is incorporated in quartz and a new (Xe,Si)O$_2$ phase is identified.

- These findings emphasize the need to consider Xe storage in crust minerals in the framework of the 'missing xenon' issue.

Abstract

Xenon (Xe), the heaviest of the stable noble gases, is missing by a factor of 20 relatively to other noble gases, when comparing the Earth's and Mars's atmospheres with chondrites. In this work, the possibility of Xe retention in quartz, a major mineral of the continental crust is tested. The Xe-SiO_2 system is investigated from 0.7 GPa to 2.7 GPa and up to 1900 K, by *in situ* X-ray powder diffraction and infrared spectroscopy. Experimental data are complemented by *ab initio* calculations to retrieve Xe incorporation mechanisms. An excess of quartz unit-cell volume up to 4.2 % is observed, consistent with a Xe for Si substitution in the quartz structure. Xe has a linear oxygen environment composed of two O atoms located at 1.98-2.00 Å from the Xe atom. Moreover, a new phase is evidenced above Xe melting curve at 0.8-1.0 GPa. The new $(Xe,Si)O_2$ phase is orthorhombic and corresponds to an elongation of the quartz unit-cell. In this phase, Xe substitutes for Si with a nearly planar oxygen environment composed of four O atoms located at 2.06-2.09 Å from the Xe atom. Xe incorporation in SiO_2 proves to be significant, as previously shown for olivine. Xe incorporation is therefore expected to occur in the whole range of lithospheric silicate minerals. These findings emphasize the need to consider Xe incorporation in crust and upper mantle minerals as a process to store and fractionate xenon, in the framework of the 'missing xenon' issue.

Keywords

1. Introduction

1.1 'Missing Xenon' and the 'Xenon paradox'

Xe is commonly used to study the evolution of the atmosphere, based on its high volatility, relative chemical inertia and its nine isotopes. However, Xe is missing in the atmospheres of Mars and of the Earth compared to chondrites, relatively to other noble gases (Anders and Owen, 1977). This phenomenon, known as the 'missing Xe' issue, is associated with a deficit in light Xe isotopes in terrestrial and martian atmospheres (Krummenacher et al., 1962 and Swindle et al., 2002 respectively), which cannot be explained by radioactive decay alone. Studies of Xe isotopic compositions of Archean rocks have shown that Xe has been fractionated throughout the Archean (e.g. Pujol et al., 2011, Avice et al., 2017). Fractionation of Xe could continue nowadays via subduction processes (Holland and Ballentine, 2006).

Several hypotheses have been proposed to explain both the 'missing Xe' and the depletion in Xe light isotopes. Early hydrodynamic escape from the atmosphere (Pépin, 1991) has been suggested although it cannot explain why noble gases, lighter than Xe, are not missing more than Xe.

Xe isotope fractionation throughout the Archean could be explained by the combination of high UV flux from the young Sun (Figure 1), and the presence of an organic haze in the early Earth's atmosphere (Hébrard and Marty, 2014). High UV flux enhances Xe photoionization at the altitude of the organic haze, Xe being preferentially ionized compared to other noble gases due to its low ionization potential. Xe is thus preferentially trapped in the organic haze,

compared to other noble gases, with adsorption process inducing Xe isotopic fractionation (Marocchi and Marty, 2013). However there is so far no clue for the presence of an organic haze in early Mars' history, and it is unclear if the UV flux, decreasing far more rapidly than Xe isotope fractionation (Figure 1) could explain Xe isotope fractionation throughout the entire Archean eon.

Xe could be stored in the core based on theoretical calculations showing that Xe could be stable up to 0.8 mol % in an iron core (Lee and Steinle-Neuman, 2006). Xe/Fe(Ni) intermetallic compounds were predicted to be stable in the core (Zhu et al., 2014), and recently synthesized (Stavrou et al., 2017). However Mars' and Earth's cores have different compositions and *P-T* conditions, which make Xe storage in the core unlikely to explain the 'missing Xe' and the depletion in light Xe isotopes observed for both planets. Jephcoat (1998) proposed the formation of molten Xe clusters during Earth differentiation, which will be driven down to the core although scarcity of Xe makes the assumption hypothetical.

Storage of Xe in sediments has also been proposed due to high Xe content retrieved in siliceous sediments (Matsuda and Matsubara, 1989), and shales (Bernatowisz, 1984), although volumes of sediments remain too small to explain the whole 'missing Xe'.

Eventually, it has been proposed that Xe could be incorporated in mantle and continental crust minerals. Xe retention in crusts and mantles could thus be at stake for both planets. High Xe reactivity has been proved, with the synthesis of several Xe compounds (Grochala, 2007), among which Xe oxides at ambient conditions (Brock and Shrobilgen, 2010), at high *P-T* conditions (Dewaele et al., 2016), and Xe-bearing perovskite (Britvin et al., 2015). Furthermore, Xe can be incorporated as a minor or trace element in SiO_2 phases (Sanloup et al., 2002, 2005), and in olivine (Sanloup et al., 2011; Crépisson et al., 2018) at upper crustal

and mantle conditions with up to 0.4 at% Xe possibly stored in olivine. However, there are still few data regarding Xe incorporation in minerals, due to Xe high volatility, which requires *in situ* investigation at high pressure (P) and temperature (T).

1.2 The Xe-SiO$_2$ system

Our previous X-ray study of the Xe-SiO$_2$ system (Sanloup et al., 2005) showed an extension of the quartz stability field and the formation of platinum silicides inside the Pt capsule attesting the release of Si from quartz. These observations led to the hypothesis that Si reduction had been triggered through Xe for Si substitution reaction. Probert (2010) investigated Xe for Si and Xe for O substitutions, as well as Xe at interstitial site in α-quartz by *ab initio* calculation using the density functional theory (DFT). All Xe incorporation mechanisms are stable at 0 GPa and 2 GPa (i.e. the two investigated P), although there is an energy barrier at $T = 0$ K. Xe incorporation in fibrous silica, studied theoretically using post-Hartree-Fock methods (Kalinowski et al., 2014), also occurs through substitution to Si surrounded by four oxygen atoms in fibrous silica, forming a stable compound well above room T.

In the present study, Xe incorporation mechanisms in α- and β-quartz are investigated experimentally and theoretically from DFT calculations. Quartz was chosen as a major mineral of the continental crust. P and T conditions are relevant for the continental crust, with highest P and T conditions relevant for orogenic contexts, where continental crust can reach 80 km depth (~2.2 GPa and 1473 K under the Tibetan plateau, Jimenez-Munt et al. (2008)).

2 Methods

2.1 X-ray diffraction

Two sets of *in situ* X-ray diffraction experiments are used here. The first set (XRD1) was collected on SiO_2 (SiO_2 as cristoballite or as Herasil glass) plus Xe gas loaded in a Pt capsule using a Paris Edinburgh cell composed of a boron epoxy gasket, with a graphite heater and hBN as the capsule container. X-ray diffraction data were collected up to 1 GPa and 1900 K at 71.68 keV on beamline ID27 at the European Synchrotron Radiation Facility (see supplementary materials in Sanloup et al. (2005) for more experimental details). Second set (XRD2) was collected on Xe/Ar-bearing quartz, synthesized in a piston cylinder press at 3.5 GPa and 1373 K for 24 hours. For this purpose silica powder was loaded with a gaseous Xe/Ar 1:1 mix in a Pt capsule following method from Boettcher et al. (1989). *In situ* X-ray diffraction data were collected up to 2.7 GPa and 900 K using resistive heating diamond anvil cells. Experiments were conducted on beamline P02.2 at Petra III synchrotron source using a 3x8 μm^2 beam at 42.7 keV. *P* was determined using unit-cell volume of a Pt grain inserted on the verge of the sample chamber, and *T* was read from a type-K thermocouple located near the diamond tip. During each measurement, the cell was oscillated from -3° to +3° to avoid intensity artefacts from potential preferential orientation. Image plates were integrated with Fit2D (Hammersley, 1997) or DIOPTAS (Prescher and Prakapenka, 2015). Le Bail refinements of crystal cell parameters were performed with GSAS software (Larson and Von Dreele, 2000).

2.2 Infrared spectroscopy

In situ IR spectra were collected on the same Xe/Ar-bearing quartz as used for XRD2, at 1.0(3) GPa and up to 773 K using resistive heating diamond anvil cells. Two chambers were drilled in a Re gasket, one was loaded with KCl used as a transparent background, and the other with a thin compressed platelet of the sample and further filled with KCl. Experiments were conducted on beamline SMIS at SOLEIL synchrotron. *P* was determined using fluorescence of a ruby sphere located in the sample chamber, and *T* was read from a type-K thermocouple located near the diamond tip. IR spectra were retrieved from 650 cm^{-1} to 4000 cm^{-1} with a resolution of 0.5 cm^{-1} and accumulation of 100 scans, repeated 4 times. A MCT detector, frequently cooled by liquid nitrogen, was used. The background used for subtraction was measured through KCl after each sample measurement. IR spectra were smoothed using Savitzki-Golay filter.

2.3. *Ab initio* calculations

All calculations were done within the density functional theory (DFT) and using the generalized gradient approximation (GGA-PBE) of Perdew et al. (1996), with the PWscf code of the Quantum espresso package http://www.quantum-espresso.org/; Gianozzi et al., 2009). The same norm-conserving pseudopotentials (Trouiller and Martins, 1991) as in Crépisson et al. (2018) are used. Electronic wave-functions (charge-density) are expanded up to an energy cut-off of 80 (480) Ry. For the new $(Xe,Si)O_2$ phase, electronic k-points sampling use a 2x4x4 centred grid for the unit-cell, and a 2x1x1 centred grid for the 1x3x3 supercell. For α-quartz unit-cell, electronic k-points sampling uses a 2x2x2-centred grid, while for the 2x2x2 and 3x3x3 supercells, calculations are restricted to the center of the Brillouin zone. These

computational parameters allow the total energy to be converged within 1mRy/atom. For all investigated systems, the charge of the simulation cell is neutral, and spin-polarized calculations were tested, obtaining zero magnetic moments. Equilibrium structures are obtained after full relaxation of atomic positions and cell parameters until convergence of forces on atoms to less than 10^{-4} Ry/au. Born effective charges are obtained within the approach of Baroni et al. (2001). Born effective charges (Z^{eff}) are used to evaluate atomic charges as discussed by Ghosez et al. (1998). Following the same procedure as Balan et al. (2011), vibrational modes and corresponding IR absorption spectra were calculated from the dynamical matrix.

3 Results and discussion

3.1 Increase of unit-cell volume in presence of Xe

As reported for olivine (Sanloup et al., 2011; Crépisson et al., 2018), the unit-cell volume of quartz is systematically larger by up to 4.2%, in presence of Xe, than the volume predicted by the equations of state of plain quartz based on *in situ* X-ray diffraction data from both XRD1 and XRD2 data sets (Table 1). Presence of Ar is unlikely to affect the unit-cell volume of quartz as Ar is classically used as a *P*-transmitting medium. For α-quartz, the excess volume presents a minimum at 468-565 K, which is the Xe melting point at the *P* of the experiment, possibly indicating a different Xe environment in α-quartz below and above Xe melting point. For β-quartz, data were all collected above Xe melting point. It is not possible to evaluate cell distortions as there is no available thermal equation of state for cell parameters of quartz at our *P-T* conditions. For α-quartz, predicted volumes are calculated

with second-order Birch Murnaghan equation of state using parameters from Wang et al. (2015), and for β-quartz, from first-order thermal Birch Murnaghan equation of state, with K_T obtained from linear interpolation of data from Dorogokupets (1995), thermal expansion from Bourova et al. (1998), and volume at 0 GPa and 848 K from Kihara (1990).

To theoretically determine Xe incorporation mechanism in quartz, two supercells were built: 2x2x2 and 3x3x3 (relative to the unit-cell of α-quartz, i.e. 9 atoms), and corresponding respectively to 1.4 at% Xe and 0.41 at% Xe. Xe for Si, Xe for O substitutions (Xe_{Si}, Xe_O), and interstitial Xe (Xe_I) were investigated. Structures were fully relaxed at 0 GPa, 1.2 GPa and 2.65 GPa. Relaxed configurations are similar at all P and Xe contents, and comparable to results from Probert (2010).

In Xe_{Si} configuration, Xe is located in a quasi-linear environment, surrounded by two O atoms at 1.98-2.00 Å (i.e. within the sum of covalent radii that Xe forms with O, ~ 2 Å) while the next two O atoms, not located in the same plane as the two closest ones, are at 2.27-2.28 Å (Figure 2a). Z^{eff} for Xe in Xe_{Si} (+ 2.8) is smaller than for Si (+ 3.4) in pure α-quartz (Table S1), which is counterbalanced by slightly less negative Z^{eff} for the four closest O atoms (Figure 2a, Table S1). In Xe_O configuration, the closest Xe neighbor is Si atom at 2.5(1) Å (i.e. within the sum of covalent radii that Xe forms with Si, ~ 2.5 Å). Z^{eff} for Xe in Xe_O (+ 0.54) significantly differs from that for O (- 1.7) in pure α-quartz (Table S1), which is counterbalanced by smaller Z^{eff} for the two closest Si, and more negative Z^{eff} for the three surrounding O compared to that for Si and O in pure α-quartz (Figure 2b, Table S1). In Xe_I configuration, we find no atoms within the sum of covalent radii that Xe forms with O or Si. Xe introduces a slight Z^{eff} excess (+ 0.13), counterbalanced by less negative Z^{eff} for the four

closest O compared to pure α-quartz (Figure 2c, Table S1). It must be noted that Z^{eff} for Xe dramatically varies as a function of the incorporation mechanism.

Occurrence of Si and O vacancies in quartz samples is suggested by water point defects (Cordier and Doukhan, 1991). Probert (2010) points out that energy formation of Si vacancy is higher than the one for O-vacancy, especially in a SiO$_2$ environment, as expected in the Earth. Nevertheless, given the very low Xe content expected inside the Earth (~ ppb), there might be anyhow enough Si-vacancies to accommodate Xe.

We therefore define formation energies for the different Xe incorporation mechanisms from a vacancy-bearing quartz:

$$\Delta E\left(Xe_{Si}\right) = E\left(Xe_{Si}\right) - E_{Xe} - E_{Qz-Si}$$

$$\Delta E\left(Xe_{O}\right) = E\left(Xe_{O}\right) - E_{Xe} - E_{Qz-O}$$

$$\Delta E(Xe_{I}) = E(Xe_{I}) - E_{Xe} - E_{Qz}$$

where $E\left(Xe_{Si}\right)$, $E\left(Xe_{O}\right)$ and $E(Xe_{I})$ are the calculated energies for the cell used to simulate the different type of incorporation mechanisms (Xe$_{Si}$, Xe$_O$ and Xe$_I$). E_{Xe} is the energy of an isolated Xe atom. E_{Qz-Si} and E_{Qz-O} are the energies of the quartz cell with one neutral Si or O vacancy (the atomic structure was fully relaxed) and E_{Qz} is the energy of a pure quartz cell.

We report calculated ΔE values at 0 GPa, 1.2 GPa, and 2.65 GPa, for models corresponding to the lowest vacancy (and Xe) concentration, i.e. for the 3x3x3 quartz supercell (Table 2). Results are consistent with those of Probert (2010): at 0 GPa we calculated $\Delta E\left(Xe_{Si}\right) = 1.0$ eV, $\Delta E\left(Xe_{O}\right) = 4.9$ eV, and $\Delta E(Xe_{I}) = 4.8$ eV against respectively 1.83 eV, 5.24 eV, and 5.24 eV for Probert (2010). At all investigated pressures, ΔE are four to five times smaller for Xe incorporation in the Si vacancy (Xe$_{Si}$) compared to interstitial

(Xe$_I$) and O-vacancy (Xe$_O$) incorporations, and as such, (Xe$_{Si}$) is the likeliest incorporation mechanism.

For 0.41 at% Xe, at 0 GPa, an increase of unit-cell volume, compared both to the bulk and to the vacancy-bearing quartz, is observed in presence of Xe for all incorporation mechanisms (Tables 3 and S2) at the exception of Xe$_{Si}$ relatively to the vacancy-bearing quartz, when a volume decrease of -0.3 % is observed. These results present significant discrepancies with Probert (2010) who calculated a decrease of volume for both Xe$_{Si}$ and Xe$_I$ relative to the bulk, and for Xe$_{Si}$ an increase of volume relative to the vacancy-bearing quartz. At 2.65 GPa we calculated an excess volume for all mechanisms relative both to bulk and vacancy-bearing quartz (+0.6% for Xe$_{Si}$, about +1.5 % for Xe$_O$, and +2.2% for Xe$_I$). These results are in agreement with Probert (2010) who calculated a volume increase of +0.42% for Xe$_{Si}$, +1.87% for Xe$_O$ and +1.7% for Xe$_I$ relatively to the bulk, at 2 GPa. The significantly smallest excess volume is obtained in the case of Xe for Si substitution, with even a decrease at 0 GPa and for 0.41 at% Xe. In line with our previous study on Xe-bearing olivine (Crépisson et al., 2018), this small excess volume as well as the formation energies suggest that Xe for Si substitution is the likeliest Xe incorporation mechanism in quartz.

α- and β-quartz structures are both hexagonal with same site multiplicities, and only differ by minor variations of bond lengths and angles (Kihara, 1990). Due to structural similarity, results from *ab initio* calculations on Xe incorporation at 0 K are thus expected to be similar for both phases, with Xe for Si substitution being the likeliest Xe incorporation mechanism.

Xe substitution to Si did not result in the formation of a pure Si phase as none was observed in the x-ray diffraction data. Indeed, while Xe was initially loaded as a gas and could initially diffuse throughout the sample, the very slow diffusion rate of Si ($\approx$ 0.2 nm to 2 nm in 24

hours, Bejina and Jaoul (1996)) prevented the formation of pure Si phase over the timescale of the experiments.

3.2 A new $(Xe,Si)O_2$ phase at high temperature

3.2.1 X-ray diffraction data

In addition to β-quartz diffraction peaks, four new peaks appeared above 1700 K at 0.8(3) GPa for XRD1 dataset, for both cristobalite and SiO_2 glass used as starting material, at interplanar distances of 2.86 Å, 2.59 Å, 2.53 Å, and 2.40 Å (Figure 3). These four new peaks correspond to continuous rings on the image plate (Figure 3), and cannot be attributed to any high-T silica phase nor to potential contamination from the Pt capsule, such as Pt_3Si observed in Sanloup et al. (2005) albeit at higher P ($P > 4$ GPa). Appearance of these four new peaks, in a very narrow interval of interplanar distances (0.5 Å), therefore attests the modification of the β-quartz structure in presence of Xe, leading to the formation of a new phase. To maximize the signal to noise ratio in the area of the new peaks, six X-ray diffraction patterns recorded at similar P-T conditions were summed.

The peaks observed in the summed pattern were indexed using DICVOL, a powder diffraction indexing software (Boultif & Louër, 1991) (Table S3). The solution of highest symmetry gives an average 2θ difference for indexed lines of 0.0018°. The solution is an orthorhombic cell with $a = 8.66(1)$ Å, $b = 5.45(1)$ Å, $c = 5.06(1)$ Å. This orthorhombic structure can be obtained by elongating β-quartz hexagonal unit-cell ($a ≈ 4.98$ Å and $c ≈ 5.45$ Å) along the b axis and by defining new axes a', b', c' so that:

$$a' = a + 2b$$

$$b' = c$$

$$c' = a$$

These relations give $a' = 8.64$ Å, $b' = 5.43$ Å and $c' = 5.00$ Å, i.e. close to the cell parameters obtained with DICVOL. The orthorhombic structure is thus considered as the likeliest based on its highest symmetry (other solutions are monoclinic), and the possibility to convert the β-quartz hexagonal structure into the orthorhombic structure by elongation. Based on extinction rules, four possible orthorhombic space groups were identified: P 2 2 2, P 2 2 2_1, Pmm2, Pmmm. For P 2 2 2_1, only one Wyckoff position is possible, hence discarding this space group.

There are 3 Si and 6 O atoms in one unit-cell of β-quartz, and consequently 6 Si and 12 O atoms are expected in the new orthorhombic cell. We use starting crystallographic structure from Kihara (1990) for β-quartz (at the highest available temperature, i.e. 1351 K) and perform symmetry operations previously described, as well as a change of the origin ($O'=O +1/2a + 1/2c$) to obtain the new atomic positions. Based on the multiplicity of Wyckoff positions, atomic positions can only be described in the P 2 2 2 space group (Table 4).

Xe incorporation occurs through Xe for Si substitution in olivine (Sanloup et al., 2011; Crépisson et al., 2018), and Xe retention in quartz was shown to release Si. Furthermore, the present *ab initio* calculations show that Xe for Si substitution is the likeliest Xe incorporation mechanism in quartz (3.1.). Therefore, we assume that Xe substitutes for Si in the new

13

orthorhombic phase, Si being present on 1c, 1h, and 4u Wyckoff positions for the new orthorhombic phase (Table 4).

The new $(Xe,Si)O_2$ phase results from the elongation of the β-quartz, similar to the formation of wadsleyite-II ($Mg_{1.71}Fe_{0.177}Al_{0.01}Si_{0.967}H_{0.332}O_4$) from wadsleyite ($β-Mg_2SiO_4$) in presence of water at 17.5 GPa and 1673 K (Smyth & Kawamoto, 1997). Wadsleyite-II has the same orthorhombic space group and the same *a* and *c* axes as wadsleyite, whereas its *b* axis is 2.5 times longer. X-ray diffraction patterns of both minerals are very similar, apart from some slight differences in peak intensities and appearance of five new peaks for wadsleyite II (Smyth et al., 2005).

-

3.2.2 *Ab initio* calculations

Xe location and occupancy in the new $(Xe,Si)O_2$ phase cannot be refined by Rietveld refinement due to the use of Sollers slits that affects peak intensity versus 2θ. Instead, *ab-initio* calculations were performed using elongated β-quartz as the starting structure (Table 4). Xe was substituted for Si on 1h, 1c, or 4u Wyckoff positions ($Xe_{Si(1h)}$, $Xe_{Si(1c)}$ or $Xe_{Si(4u)}$ respectively). Structures were fully relaxed at 0 GPa for one Xe atom per unit-cell (i.e. 5.56 at% Xe or 28.32 wt% Xe) and for a 1x3x3 supercell (i.e. 0.62 at% Xe or 5.92 wt% Xe). Indeed 36.6 wt% Xe to 38.1 wt% Xe were initially loaded in these experiments, thus we test circa maximal Xe content and a lower Xe content. It was shown that only 0.4 at% Xe can be incorporated in the olivine structure (Crépisson et al., 2018), and thus only a part of the available Xe may have been incorporated in the new $(Xe,Si)O_2$ phase.

$Xe_{Si(1h)}$, $Xe_{Si(1c)}$ lead to similar structures; 1h and 1c positions being equivalent by translation of the unit-cell. For the three sites, final total energies are similar within 0.4 eV, and the most stable configuration depends on Xe content (Table 5). Calculated volume for Xe in 1h or 1c sites is larger than for Xe in 4u site, and both are larger than experimentally determined volume. Keeping the same reasoning as before, we note that the volume increase related to the presence of Xe is smaller in the case of $Xe_{Si(4u)}$, which suggests that the crystallographic site 4u is the likeliest location.

Relaxed structures are shown in figures 4a and 4b. Xe is surrounded by four O atoms in a quasi-planar configuration, for both $Xe_{Si(1h)}$ and $Xe_{Si(4u)}$, with Xe-O bond lengths equal to 2.02-2.09 Å, i.e. close to the sum of covalent radii of Xe and O (~ 2 Å). This result is similar to predicted mechanism of Xe incorporation in fibrous silica, where Xe substituted for Si with a planar local environment formed by four oxygen atoms, and Xe-O bond lengths of 2.17 Å (Kalinowski et al., 2014). However, this result differs from Xe incorporation in olivine: although Xe also substituted for Si with a quasi-planar local environment and Xe-O bonds lengths circa 2 Å, Xe was surrounded only by three O atoms in olivine (Crépisson et al., 2018).

For $Xe_{Si(1h)}$ or $Xe_{Si(1c)}$ Z^{eff} for Xe is larger than average for Si atoms located far from Xe. Z^{eff} for the four surrounding O are also less negative than for O located far from Xe (Figure 4a). The general excess Z^{eff} is likely counterbalanced by the whole electric field of surrounding atoms. For $Xe_{Si(4u)}$ Z^{eff} for Xe is smaller than for Si atoms located far from Xe, which is counterbalanced by slightly less negative Z^{eff} for the four surrounding O, compared to that for O atoms located far from Xe (Figure 4b), similarly to what is observed for Xe for Si substitution in α-quartz (Figure 2a).

3.2.3 Infrared data

In situ infrared spectrum recorded at 1.0(3) GPa and ambient *T* compares well with that of α-quartz at ambient conditions (Figure 5) (Williams et al., 1993). Upon increasing *T*, above 473 K, a progressive splitting of the 1085 cm^{-1} band related to asymmetric stretching vibrations of SiO$_4$ tetrahedra (Williams et al., 1993) is observed (Figure 5). This is not expected for pure quartz, as IR quartz signal at 1273 K (Shoval et al., 1997) is similar to the one recorded at ambient conditions, except for a slight shift in frequency (Figure 5, Table 6). Splitting must thus be related to Xe incorporation in quartz at *T* = 473 K, i.e. just above Xe melting point (Ferreira & Lobo, 2008).

Ab initio calculations for pure α-quartz at 0 GPa are in agreement with experimental data from Williams et al. (1993) and Shoval et al. (1997) (Table 6) apart from a global shift in frequency, common to DFT calculations. Our results also agree with theoretical calculations from Méheut (2008), who used similar computational techniques (Table 6).

IR signal was calculated for Xe for Si substitution in α-quartz (Xe$_{Si}$) for 1.38 at% Xe (Figures 2a and 5). Xe$_{Si}$ in α-quartz cannot explain the observed splitting of the main 1085 cm^{-1} band despite the calculated new contributions at 30 cm^{-1} below and at 50-150 cm^{-1} above the main band, as those are too weak.

Instead, a phase transition could be at stake, as observed by X-ray diffraction (Figures 3, 4a, and 4b). To test this hypothesis, we calculated IR signal of the new (Xe,Si)O$_2$ phase for 5.56 at% Xe, for Xe$_{Si(1h)}$ and Xe$_{Si(4u)}$ configurations (Figures 4a, 4b and 5). For both configurations a splitting of the main 1085 cm^{-1} band is observed: for Xe$_{Si(1h)}$ significant

contributions appear at 50 cm⁻¹ below and 120 cm⁻¹ above the main band, and for $Xe_{Si(4u)}$ at

150 cm⁻¹ above the main band (Figure 5). IR signal of $Xe_{Si(4u)}$ compares significantly better to

the experimental IR spectra than that of $Xe_{Si(1h)}$ (Figure 5), and $Xe_{Si(4u)}$ leads to a smaller

volume increase than $Xe_{Si(1h)}$ (Table 5), thus $Xe_{Si(4u)}$ is the likeliest configuration for the new

$(Xe,Si)O_2$ phase. Transition to the new $(Xe,Si)O_2$ phase from α-quartz is not surprising due to

the similarity of α- and β-quartz structures. We note that phase transition observed by X-ray

diffraction occurred at much higher T (3.2.1) potentially controlled by diffusion of Xe which

was initially loaded as a pure phase surrounding silica, in contrast to IR data experiment

where the starting material was already Xe-doped.

4 Conclusions

Xe retention in SiO_2 at the conditions of the deep continental crust is elucidated. Xe

substitutes to Si in quartz, as in olivine (Crépisson et al., 2018). In addition to Xe

incorporation as point defects in quartz, for the first time a phase transition is observed in

presence of Xe at higher T. Occurrence of a phase transition indicates that Xe for Si

substitution is increasingly enhanced above Xe melting curve, breaking the quartz symmetry

at a macroscopic scale, thus suggesting high Xe content in the new $(Xe,Si)O_2$ phase.

Xe is incorporated in quartz at point defects bonding closely to two oxygens in a linear

configuration, while in the new $(Xe,Si)O_2$ phase Xe is bonded to four oxygens in a quasi-

planar environment. In both cases Xe-O bond lengths range from 1.98 Å to 2.09 Å, proving

that Xe-O bonds are at least partly covalent.

Xe reactivity is thus widespread in lithospheric minerals, affecting at least quartz and

olivine; quartz, the silicic end-member, being representative of the continental crust, while

17

olivine, the magnesian end-member, is representative of the lithospheric mantle. Xe reactivity is therefore expected to be ubiquitous in the lithosphere and potentially at greater depths which remains to be investigated.

Acknowledgements

References

Anders, E., & Owen, T. (1977) Mars and Earth: Origin and Abundance of volatiles. *Science* 198, 453-465.

Avice, G., Marty, B., & Burgess, R. (2017). The origin and degassing history of the Earth's atmosphere revealed by Archean xenon. *Nature Communications*, 8, 15455.

Balan, E., Ingrin, J., Delattre, S., Kovács, I., & Blanchard, M. (2011). Theoretical infrared spectrum of OH-defects in forsterite. *European Journal of Mineralogy*, 23, 285–292.

Baroni, S., de Gironcoli, S., Dal Corso, A., & Giannozzi, P. (2001). Phonons and related crystal properties from density-functional perturbation theory. *Reviews of Modern Physics*, 73, 515-562.

Béjina, F., & Jaoul, O. (1996). Silicon self-diffusion in quartz and diopside measured by nuclear micro-analysis methods. *Physics of the Earth and Planetary Interiors*, 97, 145–162.

Bernatowicz, T.J., Podosek, F.A., Honda, M., & Kramer, F.E. (1984). The atmospheric inventory of xenon and noble gases in shales: The plastic bag experiment. *Journal of Geophysical Research*, 89 (B6), 4597-4611.

Boettcher, S.L., Guo, Q., & Montana, A. (1989). A simple device for loading gases in high-pressure experiments. *American Mineralogist*, 74, 1383-1384.

Boultif, A., & Louër, D. (1991). Indexing of Powder Diffraction Patterns for Low-Symmetry Lattices by the Successive Dichotomy Method. *Journal of Applied Crystallography*, 24 (6), 987-993.

Bourova, E., & Richet, P. (1998). Quartz and Cristobalite: high-temperature cell parameters and volumes of fusion. *Geophysical Research Letters*, 25, 2333-2336.

Britvin, S., Kashtanov, A., Krzhizhanovskaya, M.G., Gurinov, A.A., Glumov, O.V., Strekopytov, S., et al. (2015). Perovskites with the Framework-Forming Xenon. *Angewandte Chemie International Edition*, 54, 14340-14344.

Brock, D.S., & Schrobilgen, G.J. (2011). Synthesis of the missing oxide of xenon, XeO_2, and its implications for Earth's missing xenon. *Journal of the American Chemical Society*, 133, 6265–6269.

Cordier P. and Doukhan J.C. Water speciation in quartz: a near infrared study (1991) American Mineralogist 76(3):361-369

Crépisson, C., Blanchard, M., Lazzeri, M., Balan, E., & Sanloup, C. (2018). New constraints on Xe incorporation mechanisms in olivine from first-principles calculations. *Geochimica et Cosmochimica Acta*, 222, 146-155.

Dewaele, A., Worth, N., Pickard, C.J., Needs, R.J., Pascarelli, S., Mathon, O., et al. (2016). Synthesis and stability of xenon oxides Xe_2O_5 and Xe_3O_2 under pressure. *Nature Chemistry*, 8 (8), 784–790.

Dorogokupets, P.I. (1995). Equation of state for lambda transition in quartz. *Journal of Geophysical Research*, 100 (B5), 8489-8499.

Ferreira, A.G.M., & Lobo, L.Q. (2008). The fusion curves of xenon, krypton, and argon. *The Journal of Chemical Thermodynamics*, 40, 618-624.

Ghosez, Ph., Michenaud, J.-P., Gonze, X. (1998). Dynamical atomic charges: the case of ABO_3 compounds. *Physical Review B*, 58, 6224-6240.

Giannozzi, P., Baroni, S., Bonini, N., Calandra, M., Car, R., Cavazzoni, et al. (2009). Quantum Espresso: a modular and open-source software project for quantum simulations of materials. *Journal of Physics: Condensed Matter*, 21, 395502-395521.

Grochala, W. (2007). Atypical compounds of gases, which have been called 'noble'. *Chemical Society Reviews*, 36, 1632-1655.

Hammersley, A. (1997). *FIT2D: An Introduction and Overview*. Technical Report N° ESRF97HA02, ESRF.

Hébrard, E., & Marty, B. (2014). Coupled noble gas-hydrocarbon evolution of the early Earth atmosphere upon solar UV irradiation. *Earth and Planetary Science Letters*, 385, 40-48.

Holland, G., & Ballentine, C.J. (2006). Seawater subduction controls the heavy noble gas composition of the mantle. *Nature*, 441, 186–191.

Jephcoat, A.P. (1998). Rare-gas solids in the Earth's deep interior. *Nature*, 393, 355-358.

Jiménez-Munt, I., Fernandez, M., Vergés, J., & Platt, J.P. (2008). Lithosphere structure underneath the Tibetan Plateau inferred from elevation, gravity, and geoid anomalies. *Earth and Planetary Science Letters*, 267, 276-289.

Kalinowski, J., Rasanen, M., & Gerber, R.B. (2014). Chemically-bound xenon in fibrous silica. *Physical Chemistry Chemical Physics*, 16, 11658–11661.

Kihara, K. (1990). An X-ray study of the temperature dependence of the quartz structure. *European Journal of Mineralogy*, 2 (1), 63-77.

Krummenacher, D., Merrihue, C.M., Pepin, R.O. & Reynolds, J.H. (1962). Meteoritic krypton and barium versus the general isotopic anomalies in xenon. *Geochimica et Cosmochimica Acta*, 26, 231–249.

Larson, A.C., & Von Dreele, R.B. (2000). General Structure Analysis System (GSAS). *Los Alamos National Report*, 86-748.

Lee, K.M., & Steinle-Neumann, G. (2006). High-pressure alloying of iron and xenon: 'Missing' Xe in the Earth's core ? *Journal of Geophysical Research*, 111, B02202.

Marrocchi, Y., & Marty, B. (2013). Experimental determination of the xenon isotopic fractionation during adsorption. *Geophysical Research Letters*, 40, 4165–4170.

Matsuda, J.-I. & Matsubara, K. (1989). Noble gases in silica and their implication for the terrestrial 'missing' Xe. *Geophysical Research Letters*, 16, 81–84.

Meheut, M. (2008). *Theoretical prediction of isotope fractionation factor between minerals, in the framework of the density functional theory*. (Doctoral dissertation). Retrieved from Tel (https://tel.archives-ouvertes.fr/tel-00231076), Sorbonne Université.

Pepin, R.O. (1991). On the Origin and Early Evolution of Terrestrial Planet Atmospheres and Meteoritic Volatiles. *Icarus* 92, 2-79.

Perdew, J.P., Burke, K., & Ernzerhof, M. (1996). Generalized gradient approximation made simple, *Physical Review Letters*, 77, 3865-3868.

Prescher, C., & Prakapenka, V.B. (2015). DIOPTAS: a program for reduction of two-dimensional X-ray diffraction data and data exploration. *High Pressure Research*, 35 (3), 223-230.

Probert, M.I.J. (2010). An *ab initio* study of xenon retention in α-quartz. *Journal of Physics: Condensed Matter*, 22, 025501-025511.

Pujol, M., Marty, B., & Burgess, R. (2011). Chondritic-like xenon trapped in Archean rocks: A possible signature of the ancient atmosphere. *Earth and Planetary Science Letters*, 308, 298–306.

Ribas, I., Guinan, E.F., Güdel, M., & Audard, M. (2005). Evolution of the Solar Activity over Time and Effects on Planetary Atmospheres. I. High−Energy Irradiances (1–1700 Å). *Astrophysical Journal*, 622 (1), 680-694.

Sanloup, C., Hemley, R.J., & Mao, HK. (2002). Evidence for xenon silicates at high pressure and temperature. *Geophysical Research Letters*, 29, 1883-1886.

Sanloup, C., Schmidt, B.C., Gudfinnsson, G., Dewaele, A., & Mezouar, M. (2011). Xenon and argon: a contrasting behavior in olivine at depth. *Geochimica et Cosmochimica Acta*, 75, 6271–6284.

Sanloup, C., Schmidt, B.C., Perez, E.C., Jambon, A., Gregoryanz, E., & Mezouar, M. (2005). Retention of xenon in quartz and Earth's missing xenon. *Science*, 310, 1174–1177.

Shoval, S., Champagnon, B., & Panczer, G. (1997). The quartz-cristobalite transformation in heated chert rock composed of micro and crypto-quartz by Micro-Raman and FTIR spectroscopy methods. *Journal of Thermal Analysis*, 50 (1-2), 203–213.

Smyth, J.R., & Kawamoto, T. (1997). Wadsleyite II: a new high pressure hydrous phase in the peridotite-H_2O system. *Earth and Planetary Science Letters*, 146, E9-E16.

Smyth, J.R., Holl, C.M., Langenhorst, F., Laustsen, H.M.S., Rossman, G.R., Kleppe, A., et al. (2005). Crystal chemistry of wadsleyite II and water in the Earth's interior. *Physics and Chemistry of Minerals*, 31, 691–705.

Stavrou, E., Yao, Y., Goncharov, A.F., Lobanov, S.S., Zaug, J.M., Liu, H., et al. (2017). Synthesis of xenon and iron-nickel intermetallic compounds at Earth's core thermodynamic conditions. *Physical Review Letters*, 120(9).

Swindle, T.D. (2002). Martian Noble Gases. *Reviews in Mineralogy and Geochemistry*, 47, 171-190.

Troullier, N., & Martins, J. L. (1991). Efficient pseudopotentials for plane-wave calculations. *Physical Review B*, 43, 1993-2006.

Wang, J., Mao, Z., Jiang, F., & Duffy, T.S. (2015). Elasticity of singlecrystal quartz to 10 GPa. *Physics and Chemistry of Minerals*, 45, 203–212.

Williams, Q., Hemley, R.J., Kruger, M.B., & Jeanloz, R. (1993). High−pressure infrared sepctra of α−quartz, coesite, stishovite and silica glass. *Journal of Geophysical Research*, 98 (B12), 22157-22170.

Zhu, L., Liu, H., Pickard, C., Zou, G., & Ma, Y. (2014). Reactions of xenon with iron and

nickel are predicted in the Earth's inner core. *Nature Chemistry*, 6, 645–649.

Table 1

Experimental quartz cell parameters and volume compared to predicted volume for plain

quartz

P (GPa)	T (K)	Cell parameters a, c (Å)	Observed V(Å³)	Predicted V (Å³)	Excess V(%)	Phase
2.65	298	4.860(1) 5.378(3)	110.00(4)	106.56	3.1	α-quartz
2.05	371	4.873(1) 5.378(3)	110.58(4)	108.03	2.3	α-quartz
1.26	468	4.893(1) 5.378(3)	111.51(3)	110.23	1.1	α-quartz
1.2	565	4.900(1) 5.392(2)	112.12(3)	110.72	1.2	α-quartz
1.62	685	4.910(1) 5.390(2)	112.51(3)	109.97	2.3	α-quartz
1.93	771	4.912(1) 5.394(2)	112.73(3)	109.39	3	α-quartz
2.55	873	4.918(1) 5.384(3)	112.80(3)	108.04	4.2	α-quartz

1.01	1591	4.976(2) 5.459(4)	117.06(4)	115.94	1.0	β-quartz
1.03	1581	4.977(2) 5.434(3)	116.44(3)	115.95	0.4	β-quartz
0.96	1651	4.977(2) 5.435(4)	116.59(4)	115.74	0.7	β-quartz
0.95	1429	4.974(9) 5.517(2)	118.22(3)	116.46	1.5	β-quartz
0.85	1520	4.981(4) 5.425(7)	116.55(1)	116.41	0.1	β-quartz

Note. Measurements on α-quartz are from XRD2 data set and those on β-quartz from XRD1 data set. For data on α-quartz, errors on P and T are 0.2 GPa and 50 K, and error on predicted volume is $\pm$ 0.5 Å^3. For β-quartz, errors on P and T are 0.3 GPa and 50 K, and error on predicted volume is $\pm$ 0.4 Å^3. Uncertainty on the last digit is given in brackets.

Table 2

Calculated energy formation ΔE as defined in the text, for Xe-doped quartz (for 0.41 at% Xe) for the three investigated Xe incorporation mechanisms.

P (GPa)	0	1.2	2.65
$\Delta E(Xe_{Si})$ (eV)	1.0	0.9	0.9
$\Delta E(Xe_O)$ (eV)	4.9	4.9	4.9
$\Delta E(Xe_I)$ (eV)	4.8	4.6	4.6

Table 3

Calculated excess volume (V) relatively to (r.t.) pure α-quartz ('r.t. bulk') or vacancy-bearing quartz ('r.t. vacancy'), for Xe-doped quartz for the three investigated Xe incorporation mechanisms.

P (GPa)	0	0	1.2	1.2	2.65	2.65
Xe content (at%)	1.4	0.41	1.4	0.41	1.4	0.41
Xe_{Si}						
excess V (% r.t. bulk)	1.6	0.4	1.8	0.6	1.9	0.6
excess V (% r.t. vacancy)	2.3	-0.3	1.0	0.4	2.1	0.6
Xe_O						
excess V (% r.t. bulk)	4.2	1.5	4.1	1.5	4.2	1.4
excess V (% r.t. vacancy)	5.4	1.8	5.1	1.8	5.1	1.6
Xe_I						
excess V (% r.t. bulk)	2.4	2.0	4.0	2.0	4.9	2.2

Table 4

Crystallographic structure found by elongation of β-quartz in the P 2 2 2 space group

SiO$_2$	Atom	x	y	Z	Wyckoff position
P 2 2 2	Si	0	½	0	1c
orthorhombic	Si	1/4	1/6	¼	4u
a = 8.66(1) Å	Si	½	½	½	1h
b = 5.45(1) Å	O	0.10	2/3	0.81	4u
c = 5.06(1) Å	O	0.60	1/3	0.69	4u
	O	0.71	0	0	2i
	O	0.79	0	½	2j

Table 5

Theoretical cell parameters, volumes and energies for Xe for Si substitutions

	$Xe_{Si(4u)}$	$Xe_{Si(1h)}$ $Xe_{Si(1c)}$	$Xe_{Si(4u)}$	$Xe_{Si(1h)}$ $Xe_{Si(1c)}$	$(Xe,Si)O_2$ phase (exp.)
at% Xe	5.56	5.56	0.62	0.62	-
a (Å)	8.75	9.41	8.74	8.93	8.66(1)
b (Å)	6.03	6.07	5.58	5.49	5.45(1)
c (Å)	4.80	4.77	5.00	5.12	5.06(1)
V (Å^3)	252.94	271.92	243.84	251.01	239 (1)
excess V (%)	6.07	14.03	2.25	5.26	-
final energy (eV)	-6189.43	-6189.00	-53280.20	-53280.64	-

Note. Results at 0 GPa, for the three possible Wyckoff positions (1h, 1c, and 4u) compared with experimental observations (exp.).

Table 6

IR active frequencies for α-quartz from experiments (exp.) and calculations (calc.)

Shoval et al. (1997), exp. at 1273 K	Williams et al. (1993), exp.	This work calc.	Méheut (2008) calc.	Mode symmetry
1166	1170	1127	1128	E
1084	1080	1031	1033	A_2
-	-	1026	1028	E
797	800	753	754	E
778	780	742	745	A_2
694	696	656	657	E

Figure 1: UV solar flux and intense Xe isotope fractionation throughout the Earth history. Extreme UV solar flux shows rapid decrease compared to progressive Xe isotope fractionation. Plain black circles are data points showing Xe isotope fractionation (references in Hébrard and Marty (2014), recent measurement from Avice et al. (2017) has been added), dashed black line is average Xe isotope fractionation. Plain red squares are solar flux data points from Ribas et al. (2005), dashed red line is a guide for the eyes.

Figure 2: Local structural and electronic environment of Xe for the three investigated incorporation mechanisms (a: Xe_{Si}, b: Xe_O, c: Xe_I). Configurations are similar for all investigated Xe contents and P. *Atomic charges (Z^{eff}) were evaluated at 0 GPa for 1.38 at%*
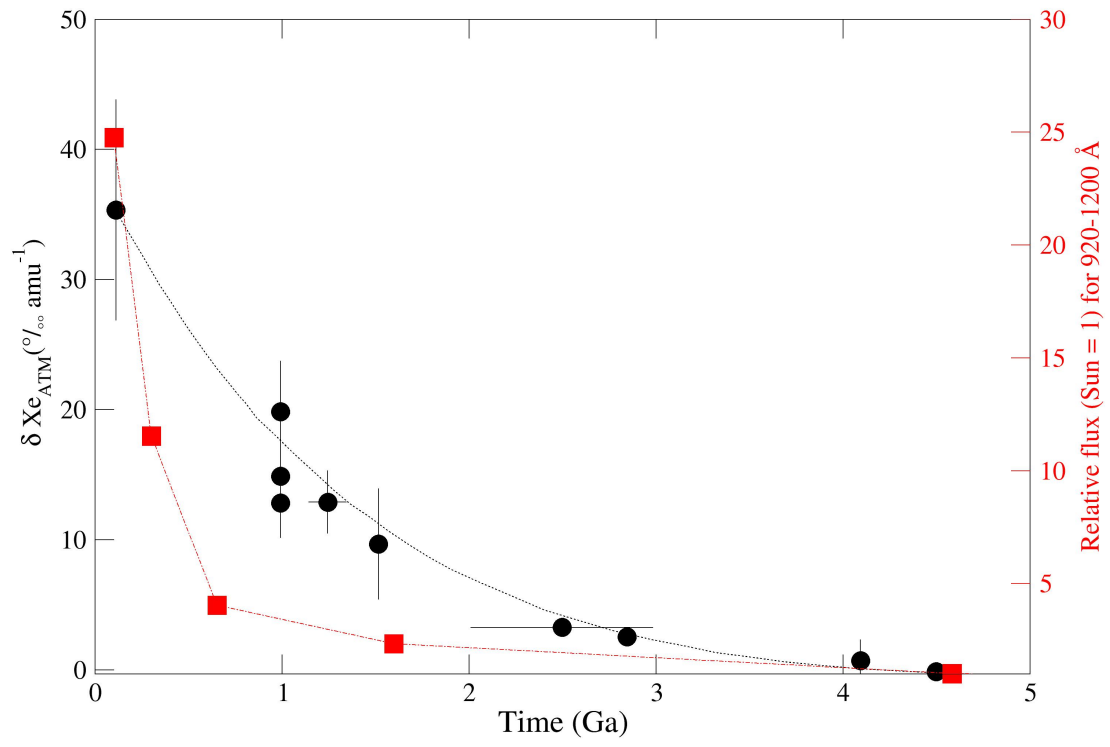
Xe while bond lengths are given for both Xe contents. Si, O and Xe are blue, red and light blue ball, respectively.

Figure 3: (left) X-ray diffraction pattern on SiO_2 + Xe at high T ($\geq$ 1700 K, XRD1). Summed X-ray diffraction pattern (black thick line) with four new peaks (red arrows) in addition to other β-quartz peaks, and hBN or platinum (Pt.) peaks from the cell assembly, also visible at low T, (green line). (right) Image plate on SiO_2 + Xe at 0.8 GPa and 1814 K with new interplanar distances. Numbers (in Å) are interplanar distances corresponding to the four new continuous rings. The very bright ring corresponds to the (002) hBN peak.

Figure 4: Relaxed structures of the new $(Xe,Si)O_2$ phase at 0 GPa with Xe in either 1h, 1c (a) or 4u (b) site. Bond lengths angles and atomic charges (Z^{eff}) are given for 5.56 at% Xe, and in brackets for 0.62 at% Xe. Si, O and Xe are blue, red and light blue ball, respectively.

Figure 5: IR spectra for the $Xe-SiO_2$ system. Experimental (exp.) IR spectra (red) recorded at high P-T conditions compared with experimental spectra for α-quartz (at 0 GPa - 1273 K from Shoval et al. (1997) and at ambient conditions from Williams et al. (1993)), calculated (calc.) spectra for α-quartz and the new $(Xe,Si)O_2$ phase.
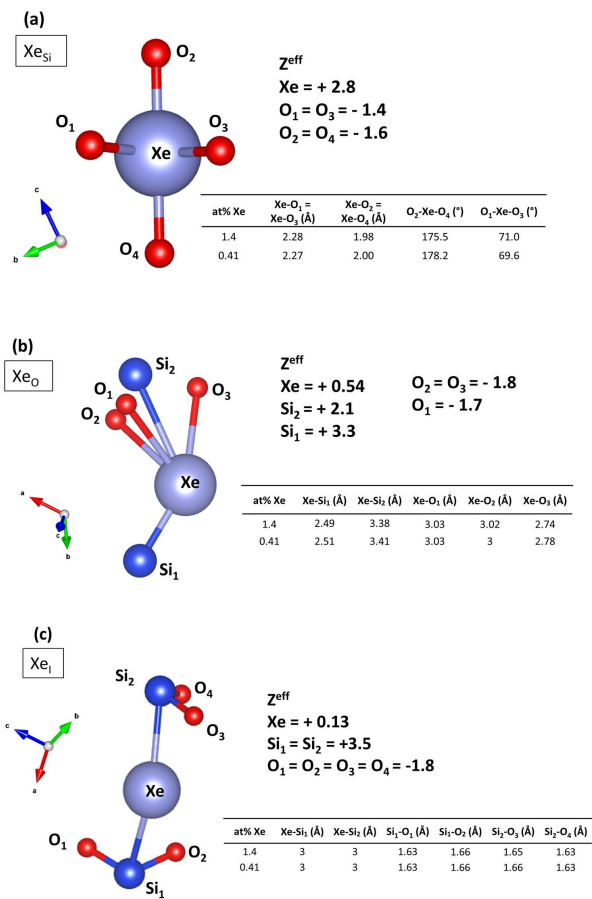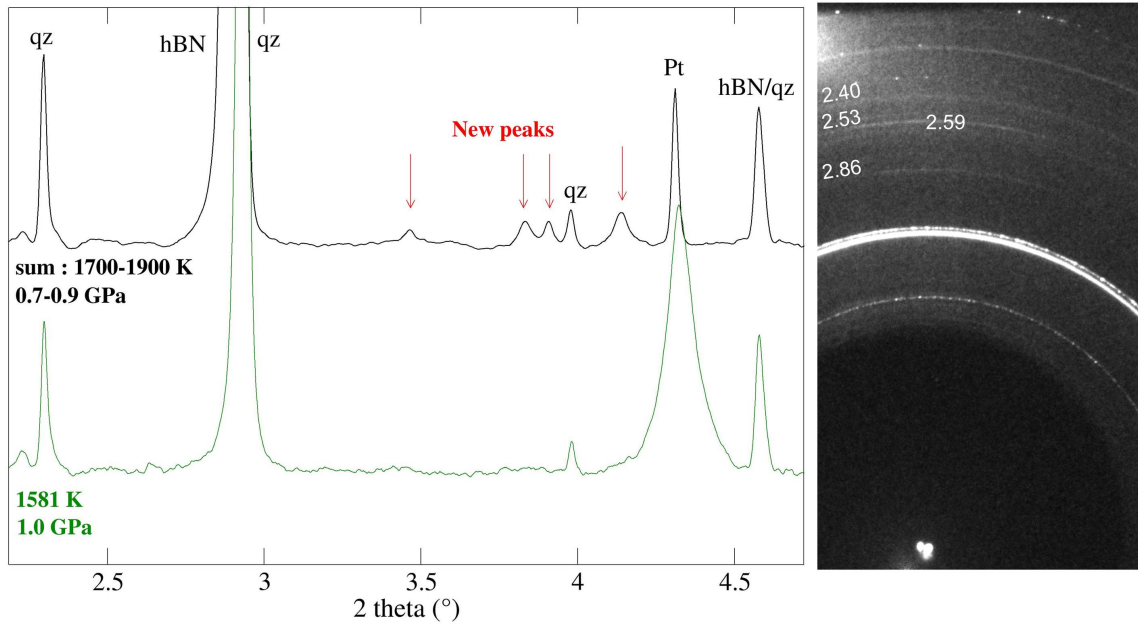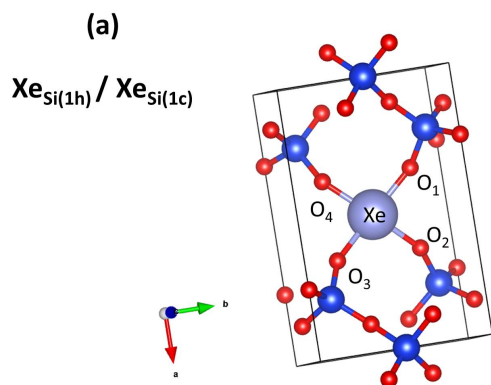
Figure 1.

(a)

Xe$_{Si}$

O$_2$

O$_1$ O$_3$

Xe

O$_4$

Z^{eff}
Xe = + 2.8
O$_1$ = O$_3$ = - 1.4
O$_2$ = O$_4$ = - 1.6

at% Xe	Xe-O$_1$ = Xe-O$_3$ (Å)	Xe-O$_2$ = Xe-O$_4$ (Å)	O$_2$-Xe-O$_4$ (°)	O$_1$-Xe-O$_3$ (°)
1.4	2.28	1.98	175.5	71.0
0.41	2.27	2.00	178.2	69.6

(b)

Xe$_O$

Si$_2$

O$_1$ O$_3$
O$_2$

Xe

Si$_1$

Z^{eff}
Xe = + 0.54
Si$_2$ = + 2.1
Si$_1$ = + 3.3

O$_2$ = O$_3$ = - 1.8
O$_1$ = - 1.7

at% Xe	Xe-Si$_1$ (Å)	Xe-Si$_2$ (Å)	Xe-O$_1$ (Å)	Xe-O$_2$ (Å)	Xe-O$_3$ (Å)
1.4	2.49	3.38	3.03	3.02	2.74
0.41	2.51	3.41	3.03	3	2.78

(c)

Xe$_I$

Si$_2$ O$_4$
O$_3$

Xe

O$_1$ O$_2$
Si$_1$

Z^{eff}
Xe = + 0.13
Si$_1$ = Si$_2$ = +3.5
O$_1$ = O$_2$ = O$_3$ = O$_4$ = -1.8

at% Xe	Xe-Si$_1$ (Å)	Xe-Si$_2$ (Å)	Si$_1$-O$_1$ (Å)	Si$_1$-O$_2$ (Å)	Si$_2$-O$_3$ (Å)	Si$_2$-O$_4$ (Å)
1.4	3	3	1.63	1.66	1.65	1.63
0.41	3	3	1.63	1.66	1.66	1.63

Figure 2.

Figure 3.

(a)

Xe$_{Si(1h)}$ / Xe$_{Si(1c)}$

Z^{eff}
Xe = + 3.84 (+3.47)
O$_1$ = O$_2$ = O$_3$ = O$_4$ = -1.85 to -1.84 (-1.61)
Si = + 3.72 to + 3.78 (+ 3.31 to + 3.48)
other O = -1.93 to -1.86 (-1.76 to -1.68)

Xe-O = 2.06 Å (2.08 Å)
O$_1$-Xe-O$_2$ = O$_3$-Xe-O$_4$ = 95.6° (94.7°)
O$_4$-Xe-O$_1$ = O$_2$-Xe-O$_3$ = 86.0° (84.4°)
O$_1$-Xe-O$_3$ = O$_4$-Xe-O$_2$ = 166.7° (164.4°)

(b)

Xe$_{Si(4u)}$
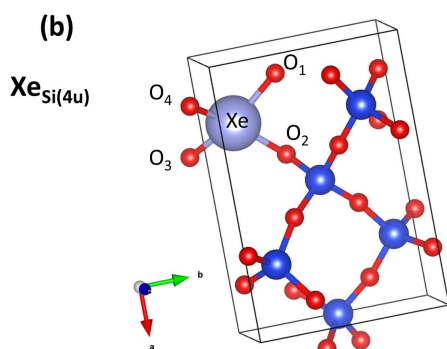
Z^{eff}
Xe = + 3.45 (+ 3.21)
O$_1$ = O$_2$ = O$_3$ = O$_4$ = -1.68 (-1.50 to -1.48)
Si = + 3.64 to + 3.75 (+ 3.28 to + 3.66)
other O = -1.99 to -1.75 (-1.91 to -1.64)

Xe-O$_1$ = Xe-O$_2$ = 2.07 Å (2.09 Å)
Xe-O$_3$ = 2.03 Å (2.08 Å)
Xe-O$_4$ = 2.03 Å (2.09 Å)
O$_4$-Xe-O$_1$ = 94.8° (96.6°)
O$_3$-Xe-O$_2$ = 94.8° (94.3°)
O$_1$-Xe-O$_2$ = 85.8° (89.1°)
O$_3$-Xe-O$_4$ = 93.3° (91.2°)
O$_1$-Xe-O$_3$ = 157.2° (154.7°)
O$_2$-Xe-O$_4$ = 157.2° (154.3°)

Figure 4.

38

Figure 5.